Analysis and Comparison of Integrated Planar Transformers for 22-kW On-Board Chargers

Tianlong Yuan, *Graduate Student Member, IEEE*, Feng Jin, *Member, IEEE*, and Qiang Li, *Member, IEEE*

***Abstract*—The surge in electric vehicle technology has brought attention to the manufacturing and design of 22-kW on-board chargers using printed circuit boards (PCBs), owing to their manufacturability and compact nature. However, designing transformers for these applications is challenging due to the demands of higher power and a smaller profile. The challenges include achieving optimal current distribution in parallel windings and easier transformer structure with better thermal performance. In addition, the integration of resonant inductance is crucial for regulatory functions and higher power densities. The integration with parallel windings also impacts the overall transformer performance, which needs to be analyzed. This article presents a detailed analysis and design approach for a 22-kW PCB-based transformer with good current sharing, controllable leakage inductance, and a simplified core structure. The study also includes an in-depth analysis of the transformer's flux distribution to minimize core loss. A 22-kW CLLC resonant converter is developed to validate the proposed transformer using PCB-packaged devices. With its modified flux distribution and good current sharing, the integrated transformer enables the converter to achieve a power density of 11.6 kW/L and a peak efficiency of 98.5%.**

***Index Terms*—CLLC, onboard charger (OBC), planar magnetics.**

I. Introduction

THE evolution of wide-band-gap (WBG) devices has ushered in a new era marked by higher power and frequencies for power converters, notably in applications like on-board chargers (OBCs). Fig. 1 illustrates a typical OBC structure, where the dc/dc stage operates between the power factor correction (PFC) stage and batteries, ensuring isolation and voltage regulation. Existing literature showcases notable efforts in the design of 6.6-kW OBCs utilizing various resonant converters such as CLLC, LLC, and LCL [1], [2], [3]. In [4], an 11-kW OBC is designed with integrated planar magnetics and a CLLC resonant converter. Among all the excellent work, designs with integrated planar magnetics have higher power density and competitive efficiency. However, research on 22-kW OBCs, especially those incorporating integrated planar magnetics, remains limited [5], [6]. Several challenges must be solved if planar integrated magnetics are used in a 22-kW converter.

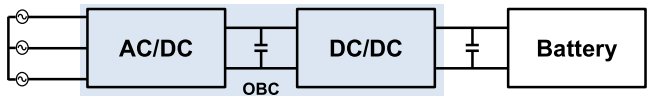

Fig. 1. Typical OBC structure.

A pivotal challenge lies in mitigating the current stress on PCB windings using parallel winding configurations. Ensuring consistent current sharing is essential [7], [8], [9], [10], [11], [12], [13], [14]. Previous studies have explored the current distribution between parallel windings related to frequency, FR4 layer thickness, and winding arrangement. Effective solutions include a sandwich structure with parallel secondary side windings on the top and bottom and primary windings in the middle [8]. Then, Chen et al. [9] gave a lumped model to predict current distribution and winding resistance, and the symmetric structure is confirmed to offer optimal current distribution. Adjustments in winding distances have proven effective in achieving uniform current sharing [10]. Innovations like planar Litz winding have been introduced to mimic the twisting of Litz wires in PCB windings [11]. While these methods achieve perfect current sharing, careful winding designs, and considering air gap impacts are essential.

In higher power applications, strategies such as interleaving transformers [12] and active current-sharing methods, compensating voltage differences on resonant inductances by adding a voltage source, have been explored [13]. However, these methods often treat the converter solely as a dc transformer without the integration and control of resonant inductances. Current distribution analysis models for Litz wire have been proposed [14], yet adapting these methods for PCB windings necessitates careful consideration of transformer structures to enhance thermal management.

Simultaneously, the integration of resonant inductors has undergone extensive exploration. Integrating resonant inductance into the air, controlled by distances between primary and secondary windings, has been investigated [15], [16]. However, this method, suitable for litz wire magnetics, faces limitations due to inherent structure and high winding loss, limiting its efficacy for PCB windings. To address these challenges, resonant inductance has been integrated into an EI core transformer using unbalanced winding structures and an additional center leg

Manuscript received 5 March 2024; revised 25 April 2024; accepted 3 June 2024. Date of publication 6 June 2024; date of current version 16 July 2024. This work was supported by AT&S and the Power Management Consortium in CPES, Virginia Tech. Recommended for publication by Associate Editor C. Chen. *(Corresponding author: Qiang Li.)*

The authors are with the CPES, Virginia Tech, Blacksburg, VA 24060 USA (e-mail: tianlong@vt.edu; fengjin@vt.edu; lqvt@vt.edu).

Color versions of one or more figures in this article are available at https://doi.org/10.1109/TPEL.2024.3410878.

Digital Object Identifier 10.1109/TPEL.2024.3410878

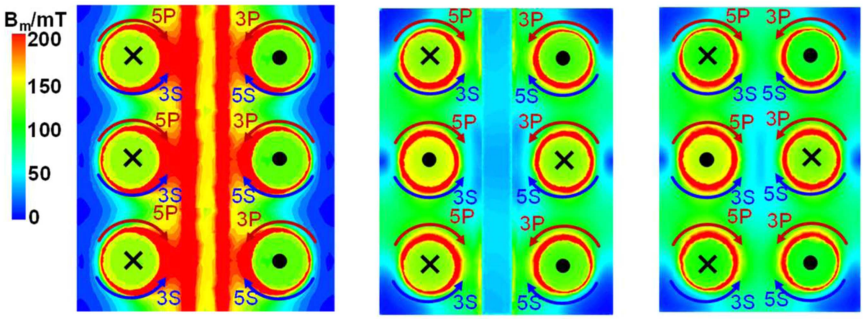

Fig. 2. Maximum flux density distributions of integrated transformers.

[17]. Although this configuration significantly increases leakage inductance, flux in the center leg results in higher core losses. Innovations such as integrating two EI cores and replacing center legs with outer legs have been explored [18]. Another approach integrates three EI cores in series connections, removing center legs due to flux cancellation and reducing core losses and high power density [4]. If the EI cores are integrated directly as shown in Fig. 2(a), high flux density in the center leg is still observed. However, the flux in the center leg is canceled if the flux direction in the center EI core is reversed as shown in Fig. 2(b). Due to the low flux density in the center leg, the resonant inductance can still be integrated into the transformer without the center leg as shown in Fig. 2(c). The flux density and core loss are greatly reduced. However, only the leakage inductance integration concept is explained, and detailed flux analysis is not carried out. The inductance analysis with parallel windings is also vacant for higher power applications. The core arrangement guideline with more core legs is also not discussed.

This article addresses the challenges mentioned in the transformer design for 22-kW OBCs. The contributions are summarized as follows.

First, various planar transformer candidates are presented and thoroughly compared for 22-kW OBCs. Integration's impact on the transformer characteristics is analyzed, including the coupling between the windings, inductance, and flux distributions. Different numbers of parallel windings are also compared. The most promising candidate is chosen for the application.

Second, a general integrated transformer with good scalability is introduced and analyzed. The current sharing can be controlled without additional complexity so that better thermal balance is realized between the parallel windings. The resonant inductance is also integrated and controlled. The exposed windings give thermal management design more possibilities with a simple core structure.

Third, this article conducts a comprehensive analysis and comparison of the proposed matrix transformers' arrangements. Detailed flux analysis and loss comparison are carried out. The guideline with the smallest core loss is given.

Fourth, detailed design procedures are given for a 22-kW CLLC resonant converter utilizing the introduced transformer. The converter also uses PCB-packaged silicon carbide (SiC) devices and has proven its performance for high-power applications [19].

TABLE I
KEY PARAMETERS OF THE CONVERTER

V_{bus}	V_o	P_{max}	f_r	I_{max}
650 V–850 V	550 V– 850 V	22 kW	250 kHz	30 A

The topology of the whole OBC is shown in Fig. 3. Three-phase totem pole PFC is used as the ac/dc stage. CLLC resonant converter is used as the dc/dc stage, which is mainly analyzed in this article. The essential parameters are detailed in Table I.

The rest of this article is organized as follows. Section II compares different integration candidates for parallel windings and selects the best candidate for this application. Section III gives the analysis of a general scalable transformer, including transformer decoupling conditions, analysis of different transformer configurations, and arrangement optimization of the matrix transformers. Section IV gives the detailed design procedure of a 22-kW CLLC resonant converter with the proposed integrated matrix transformer. Section V presents the hardware and the experimental results. Finally, Section VI concludes this article, summarizing key findings and suggesting directions for future research.

II. Analysis and Comparison of Transformer Candidates for 22-kW OBC Applications

This chapter lists and compares all the possible transformer candidates for 22-kW OBC applications. The analysis and comparison mainly focus on the inductance values, flux distribution, and loss information.

A. Candidate I: Separate Parallel Transformers

The first instinct is to use two 11-kW transformers for a 22-kW prototype or use two 11-kW converters in parallel. For one 22-kW prototype, only a minimum of eight devices are needed if the devices can handle such a high current. Also, the corresponding gate drivers and auxiliary supplies are fewer. The maximum switching frequency of a 22-kW prototype is also lower because of its heavier load. So, one 22-kW prototype with two 11-kW transformers is better for the application due to

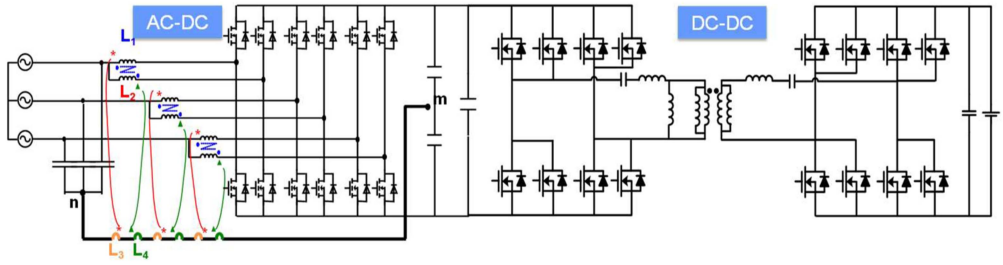

Fig. 3. Structure of the 22-kW OBC system.

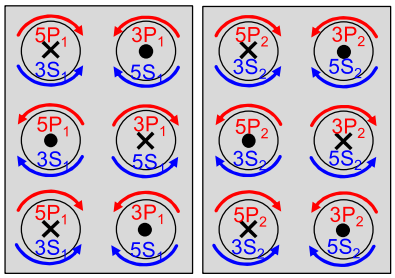

Fig. 4. Candidate I: Separate parallel transformers.

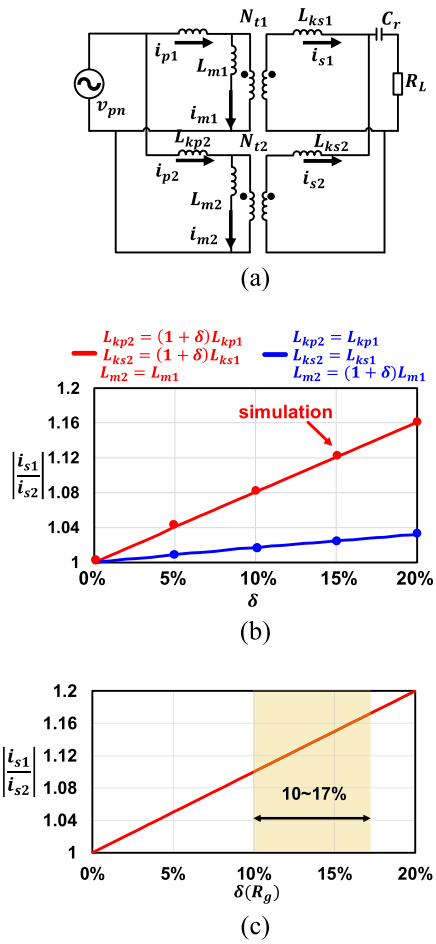

Fig. 5. (a) Circuit model for parallel transformers. (b) Current distribution for different perturbations on inductance values. (c) Current distribution for perturbation on air gaps.

its lower cost, lower maximum switching frequency, and easier current sharing control. The transformer structure is shown in Fig. 4. The red arrows represent the current direction of the primary current. The blue arrows represent the current direction of the secondary current. The three legs on the left have five primary turns and three secondary turns. The three legs on the right have five secondary turns and three primary turns.

While using parallel windings, the current distribution, which is impacted by the inductance values of the parallel transformers, cannot be neglected. The circuit model to analyze the two parallel transformers is shown in Fig. 5. Since only the current distribution information is needed, the calculation and analysis only start from the point where parallel windings are introduced and end at the load. Based on KVL and KCL, (1)–(3) can be derived, where v_{pn} is the primary voltage over the nth transformer, i_{pn} and i_{sn} are the primary and secondary current in the nth transformer, L_{kpn}, L_{ksn}, and L_{mn} are the primary leakage inductance, secondary inductance, and magnetizing inductance of the nth transformer, R_L is the equivalent load resistor calculated in (4), and C_r is the resonant capacitance value. Then, the current distribution can be calculated in (5). $K_{1,n}$, $K_{2,n}$, and $K_{3,n}$ are the parameters defined in (6)–(8). The results of the amplitude at the nominal condition are shown in Fig. 5(b), where δ is the difference introduced to the inductances. The calculated results match well with the simulation results. The leakage inductances have a more significant impact on the current distribution. The impact of magnetizing inductance is relatively tiny

$$v_{pn} = sL_{kpn}i_{pn} + sL_{mn}i_{mn} \tag{1}$$

$$i_{pn} = i_{sn} + i_{mn} \tag{2}$$

$$\sum_{n=1}^{2} i_{sn}\left(R_L + \frac{1}{sC_r}\right) = fracsL_{mn}i_{mn}N_{tn} - sL_{ksn}i_{sn} \tag{3}$$

$$R_L = 8R_o/\pi^2 \tag{4}$$

$$\frac{i_{s1}}{i_{s2}} = \frac{N_{t1}\left(K_{1,2}L_{m1}C_r s^2 + K_{2,2}s + K_{3,2}\right)}{N_{t2}\left(K_{1,1}L_{m2}C_r s^2 - K_{2,1}s - K_{3,1}\right)} \tag{5}$$

$$K_{1,n} = L_{mn}\, L_{kpn} + N_{tn}^2 L_{ksn} L_{pn} \tag{6}$$

$$K_{2,n} = C_r\, R_L\left[N_{tn}L_{m1}L_{m2}\left(N_{t2} - N_{t1}\right) + K_{3,n}\right] \tag{7}$$

$$K_{3,n} = N_{t,n}\,\left[L_{m1}N_{t2}L_{p2} - L_{m2}N_{t1}L_{p1}\right]. \tag{8}$$

The magnetizing inductance and leakage inductance are calculated in (9) and (10), where R_g is the reluctance of the air gap. Because of the consistency of the PCB manufacturing, the air gap

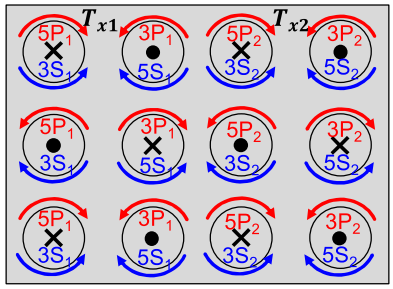

Fig. 6. Candidate II: Integrated transformer with negative coupling.

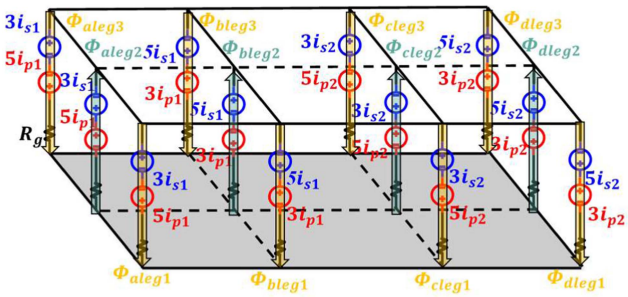

Fig. 7. Reluctance model for candidate II.

has the most impact on the current distribution. Fig. 5(c) shows the current amplitude distribution of the parallel transformers with perturbation $\delta(R_g)$ on the air gaps at the nominal condition. From the figure, the current distribution is almost in a linear relationship with the magnetic reluctance. In mass production, the difference in the air gaps between transformers is around 10% to 17%, so the perfect current sharing is hard to achieve. However, the air gaps are almost the same within one transformer, so the integrated transformer solutions are introduced in the following paragraphs for perfect current distribution

$$L_m = \frac{272}{3R_g} \tag{9}$$

$$L_{kp} = L_{ks} = \frac{32}{3R_g}. \tag{10}$$

B. Candidate II: Integrated Transformer With Negative Coupling

To have a better current distribution, the two transformers in candidate I are integrated on the same plate. The transformer structure is shown in Fig. 6. Subscript one means the windings for the transformer T_{x1}. Subscript two means the windings for the transformer T_{x2}. The reluctance model of the transformer is shown in Fig. 7. From the reluctance model, the inductance matrix is calculated in (11), where v_{p1} and v_{s1} are the voltages on the primary and secondary windings of T_{x1}, v_{p2} and v_{s2} are the voltages on the primary and secondary windings of T_{x2}, ${i_{p1}}'$ and ${i_{s1}}'$ are the differential of the primary and secondary current with respect to time of T_{x1}, ${i_{p2}}'$ and ${i_{s2}}'$ are the differential of the primary and secondary current with respect to time of T_{x2}. From

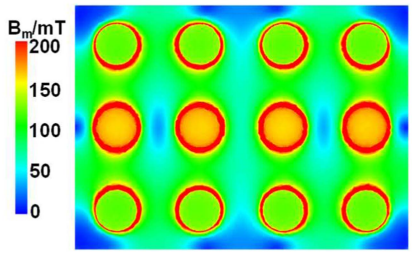

Fig. 8. Flux distribution of candidate II.

(11), it can be found that the two parallel windings are negatively coupled. This is because the magnetic motive force (MMF) of T_{x1} and T_{x2} are in opposite directions for the corresponding legs. The magnetizing inductance and the leakage inductance of the integrated transformer with parallel windings can be further calculated in (12) and (13), with detailed calculations in Appendix I. From (12) and (13), the ratio of magnetizing inductance over the leakage inductance, L_n is 8.5, which is the same as separate transformers. The simulated L_n value is 8.4, which is 1.2% smaller than the calculated result.

$$\begin{bmatrix} v_{p1} \\ v_{s1} \\ v_{p2} \\ v_{s2} \end{bmatrix} = \begin{bmatrix} \frac{305}{3R_g} & -\frac{271}{3R_g} & -\frac{1}{3R_g} & -\frac{1}{3R_g} \\ -\frac{271}{3R_g} & \frac{305}{3R_g} & -\frac{1}{3R_g} & -\frac{1}{3R_g} \\ -\frac{1}{3R_g} & -\frac{1}{3R_g} & \frac{305}{3R_g} & -\frac{271}{3R_g} \\ -\frac{1}{3R_g} & -\frac{1}{3R_g} & -\frac{271}{3R_g} & \frac{305}{3R_g} \end{bmatrix} \begin{bmatrix} {i_{p1}}' \\ {i_{s1}}' \\ {i_{p2}}' \\ {i_{s2}}' \end{bmatrix} \tag{11}$$

$$L_m = \frac{136}{3R_g} \tag{12}$$

$$L_{kp} = L_{ks} = \frac{16}{3R_g}. \tag{13}$$

The flux in each leg can be calculated in (14) and (15), where Φ_{aleg1} and Φ_{aleg3} are the flux through the outer legs, and Φ_{aleg2} is the flux through the inner leg shown in Fig. 7. The flux difference between the outer legs and the center leg is calculated in (16). According to (16), the center leg has a stronger flux density, and the difference will become larger with parallel windings. The simulated maximum flux density distribution is shown in Fig. 8

$$\Phi_{aleg1} = \Phi_{aleg3} = \frac{29}{6R_g} i_{p1} - \frac{19}{6R_g} i_{s1} - \frac{1}{6R_g} (i_{p2} + i_{s2}) \tag{14}$$

$$\Phi_{aleg2} = \frac{31}{6R_g} i_{p1} - \frac{17}{6R_g} i_{s1} + \frac{1}{6R_g} (i_{p2} + i_{s2}) \tag{15}$$

$$\Phi_{diff} = \frac{i_{p1} + i_{p2} + i_{s1} + i_{s2}}{3R_g}. \tag{16}$$

The flux in each leg can be rewritten into the form shown in (17) and (18), where Φ_a and Φ_b are calculated in (19) and (20). Then the core loss on the three legs, P_{legs_real}, can be calculated in (21), where C_m, α, and β are the parameters from Steinmetz equation, f is the operating frequency, V_{leg} is the volume of each

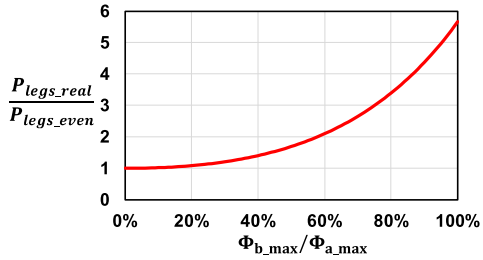

Fig. 9. Real core loss on legs versus flux difference on legs.

core leg, B_{m1} and B_{m2} are the maximum flux density calculated in (22) and (23), A_e is the cross-section area of each core leg. The same calculation can be applied to the core legs in the other arrays

$$\Phi_{aleg1} = \Phi_{aleg3} = \Phi_a - \Phi_b \tag{17}$$

$$\Phi_{aleg2} = \Phi_a + \Phi_b \tag{18}$$

$$\Phi_a = \frac{30}{6R_g} i_{p1} - \frac{18}{6R_g} i_{s1} \tag{19}$$

$$\Phi_b = \frac{1}{6R_g} (i_{p1} + i_{s1} + i_{p2} + i_{s2}) \tag{20}$$

$$P_{legs\_real} = 2C_m f^{\alpha} B_{m1}^{\beta} V_{leg} + C_m f^{\alpha} B_{m2}^{\beta} V_{leg} \tag{21}$$

$$B_{m1} = \max\left(\frac{\Phi_a - \Phi_b}{A_e}\right) \tag{22}$$

$$B_{m2} = \max\left(\frac{\Phi_a + \Phi_b}{A_e}\right). \tag{23}$$

If the flux in each leg is the same within one array, the maximum flux density can be calculated in (24) with the same voltage excited on the winding. Then, the core loss on the legs in one array is calculated in (25). Fig. 9 shows the relation between $P_{\text{legs\_real}}/P_{\text{legs\_even}}$ and $\Phi_{b\_\max}/\Phi_{a\_\max}$. $P_{\text{legs\_real}}$ is the real core loss on the legs with uneven flux distribution shown in Fig. 8. $P_{\text{legs\_even}}$ is the optimal core loss on the legs when the flux is evenly distributed among the legs. According to the figure, the total core loss on the legs is the smallest if the flux is evenly distributed among all the legs with the same current excitation and voltage across the windings. Fig. 9 is only used to prove that evenly distributed flux is better from a core loss point of view under the same voltage and current excitations. However, this is not achievable under this structure

$$B_m = \max\left(\frac{\Phi_a - \Phi_b/3}{A_e}\right) \tag{24}$$

$$P_{\text{legs\_even}} = 3C_m f^{\alpha} B_m^{\beta} V_{\text{leg}}. \tag{25}$$

C. Candidate III: Integrated Transformer With Positive Coupling

To have evenly distributed flux among the legs, candidate III is introduced by reversing the flux directions of T_{x2} as shown in Fig. 10. The flux in the legs are calculated in (26) and (27). If perfect current sharing is realized, the flux in the outer legs is the same as the inner legs but with opposite directions, as calculated in (28)

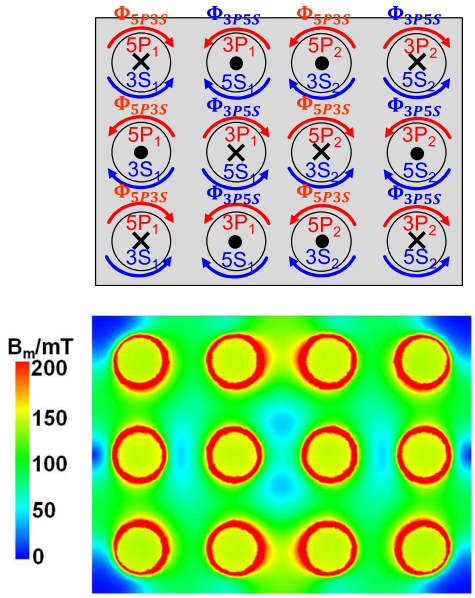

Fig. 10. Candidate III: Integrated transformer with positive coupling and its flux distribution (case I).

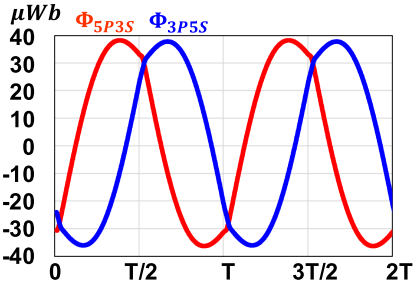

Fig. 11. Flux versus time for the two types of legs.

$$\Phi_{aleg1} = \Phi_{sleg3} = \frac{29}{6R_g} i_{p1} - \frac{19}{6R_g} i_{s1} + \frac{1}{6R_g} (i_{p2} + i_{s2}) \tag{26}$$

$$\Phi_{aleg2} = \frac{31}{6R_g} i_{p1} - \frac{17}{6R_g} i_{s1} - \frac{1}{6R_g} (i_{p2} + i_{s2}) \tag{27}$$

$$\Phi_{aleg1} = \Phi_{aleg2} = \Phi_{aleg3} = \frac{5}{R_g} i_{p1} - \frac{3}{R_g} i_{s1}. \tag{28}$$

For the most optimized core loss, the flux distribution on the core plate also needs to be considered. For candidate III, only two types of legs are included: legs with five primary windings and three secondary windings and legs with three primary windings and five secondary windings. The flux of these two types of legs are calculated in (29) and (30) with directions shown in Fig. 10. The flux versus time is plotted in Fig. 11. To have a lower core loss on the plate, the most effective arrangement is achieved when the flux in one leg consistently opposes the flux

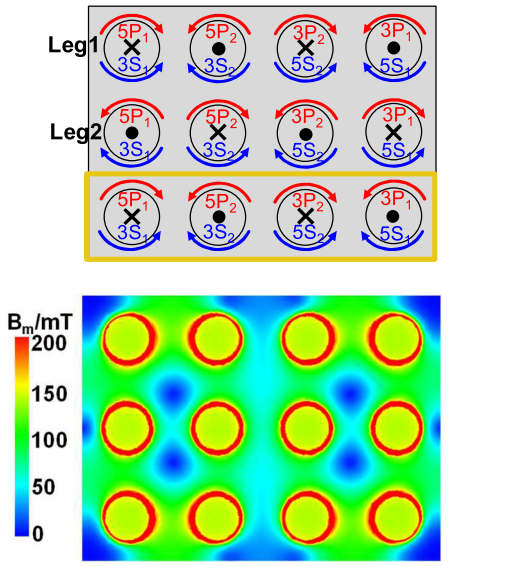

Fig. 12. Candidate III: Integrated transformer with positive coupling and its flux distribution (case II).

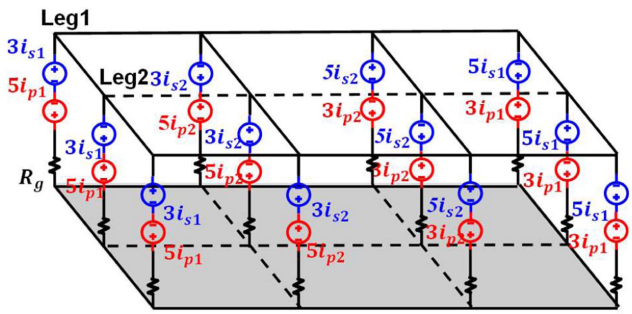

Fig. 13. Reluctance model of case II.

in all surrounding legs. Therefore, the arrangement depicted in Fig. 12 is proposed, where legs of the same type are positioned adjacent to each other but in opposite directions noted as case II. This approach reduces the core loss by 17%, dropping from 98 to 81 W

$$\Phi_{5P3S} = \frac{5}{R_g}\, i_{p1} - \frac{3}{R_g} i_{s1} \tag{29}$$

$$\Phi_{3P5S} = \frac{5}{R_g}\, i_{s1} - \frac{3}{R_g} i_{p1}. \tag{30}$$

The reluctance model of the optimized transformer case II is shown in Fig. 13. The inductance matrix can be calculated in (31). From (31), the two parallel windings are positively coupled. The magnetizing inductance and the leakage inductance of the transformer are calculated in (32) and (33). The L_n of candidate III is 7.5, which is different from separate transformers because of the coupling. The simulated L_n value is also 7.5, which is the same as the calculations

$$\begin{bmatrix} v_{p1} \\ v_{s1} \\ v_{p2} \\ v_{s2} \end{bmatrix} = s \begin{bmatrix} \frac{305}{3R_g} & -\frac{271}{3R_g} & \frac{1}{3R_g} & \frac{1}{3R_g} \\ -\frac{271}{3R_g} & \frac{305}{3R_g} & \frac{1}{3R_g} & \frac{1}{3R_g} \\ \frac{1}{3R_g} & \frac{1}{3R_g} & \frac{305}{3R_g} & -\frac{271}{3R_g} \\ \frac{1}{3R_g} & \frac{1}{3R_g} & -\frac{271}{3R_g} & \frac{305}{3R_g} \end{bmatrix} \begin{bmatrix} i_{p1}{}' \\ i_{s1}{}' \\ i_{p2}{}' \\ i_{s2}{}' \end{bmatrix} \tag{31}$$

$$L_m = \frac{45}{R_g} \tag{32}$$

$$L_{kp} = L_{ks} = \frac{6}{R_g}\,. \tag{33}$$

D. Candidate IV: Integrated Transformer With Decoupled Parallel Windings

Based on the previous analysis, the parallel windings are negatively coupled with candidate II and positively coupled with candidate III. This paragraph will derive candidates without coupling between the parallel windings for a comprehensive comparison.

From Figs. 12 and 13, Leg1 and Leg2 have the same MMF in opposite directions. So, their total MMF excitations on the other legs is zero. If MMF is excited on Leg1 and Leg2 from other legs, the voltages excited on the windings around Leg1 and Leg2 have the same amount with opposite directions. Therefore, if Leg1 and Leg2 are considered as one transformer, it will be decoupled from the other legs. For candidate III, the legs that do not meet the previous analysis are in the yellow block shown in Fig. 12. The parallel windings could decouple from each other by modifying the winding arrangements in the block.

The first way is to change the winding arrangements, as shown in Fig. 14 noted as case I. The inductance matrix for the transformer in Fig. 14 is calculated in (34). The parallel windings are decoupled from each other. Then, the magnetizing inductance and leakage inductance are calculated in (35) and (36). The simulated L_n value is also 11.5, which is the same as the calculations

$$\begin{bmatrix} v_{p1} \\ v_{s1} \\ v_{p2} \\ v_{s2} \end{bmatrix} = s \begin{bmatrix} \frac{100}{R_g} & -\frac{92}{R_g} & 0 & 0 \\ -\frac{92}{R_g} & \frac{100}{R_g} & 0 & 0 \\ 0 & 0 & \frac{100}{R_g} & -\frac{92}{R_g} \\ 0 & 0 & -\frac{92}{R_g} & \frac{100}{R_g} \end{bmatrix} \begin{bmatrix} i_{p1}{}' \\ i_{s1}{}' \\ i_{p2}{}' \\ i_{s2}{}' \end{bmatrix} \tag{34}$$

$$L_m = \frac{46}{R_g} \tag{35}$$

$$L_{kp} = L_{ks} = \frac{4}{R_g}\,. \tag{36}$$

The second way is to eliminate the coupled legs as shown in Fig. 15 noted as case II. The inductance matrix of the transformer shown in Fig. 15 is calculated in (37). The magnetizing inductance and leakage inductance are calculated in

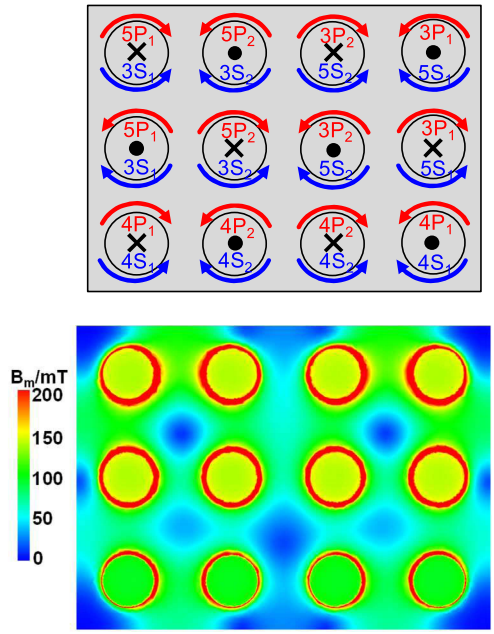

Fig. 14. Candidate IV: Integrated transformer with decoupling and its flux distribution (case I).

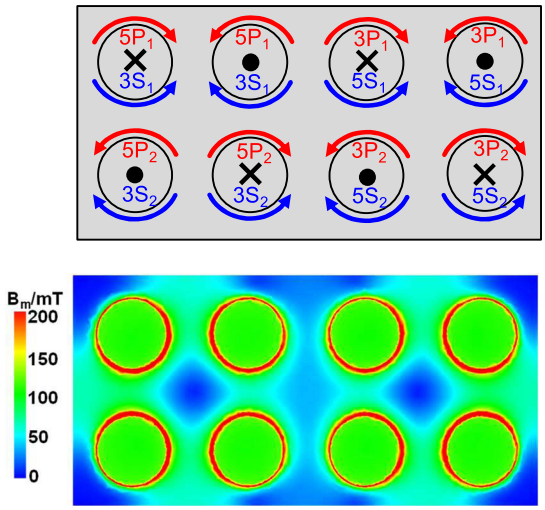

Fig. 15. Candidate IV: Integrated transformer with decoupling and its flux distribution (case II).

(38) and (39)

$$\begin{bmatrix} v_{p1} \\ v_{s1} \\ v_{p2} \\ v_{s2} \end{bmatrix} = s \begin{bmatrix} \frac{68}{R_g} & -\frac{60}{R_g} & 0 & 0 \\ -\frac{60}{R_g} & \frac{68}{R_g} & 0 & 0 \\ 0 & 0 & \frac{68}{R_g} & -\frac{60}{R_g} \\ 0 & 0 & -\frac{60}{R_g} & \frac{68}{R_g} \end{bmatrix} \begin{bmatrix} {i_{p1}}' \\ {i_{s1}}' \\ {i_{p2}}' \\ {i_{s2}}' \end{bmatrix} \tag{37}$$

$$L_m = \frac{30}{R_g} \tag{38}$$

$$L_{kp} = L_{ks} = \frac{4}{R_g}. \tag{39}$$

TABLE II
COMPARISON BETWEEN THE TWO DECOUPLED TRANSFORMER

	L_m	L_k	Core loss	Winding loss	Footprint
Case I	$33\mu H$	$2.9\mu H$	65 W	93 W	12463 mm^2
Case II	$33\mu H$	$4.4\mu H$	80 W	80 W	12480 mm^2

TABLE III
PARAMETERS OF ALL THE CANDIDATES

	L_m	L_k	Core loss	Winding loss	Footprint
Cand. I	33 μH	3.8 μH	82 W	98 W	12463 mm^2
Cand. II	33 μH	3.8 μH	81 W	98 W	12463 mm^2
Cand. III	33 μH	4.4 μH	81 W	98 W	12463 mm^2
Cand. IV	33 μH	4.4 μH	80 W	80 W	12480 mm^2

TABLE IV
PARAMETERS OF TRANSFORMERS WITH DIFFERENT PARALLEL WINDINGS

No. para	L_m	L_k	Core loss	Winding loss	Footprint
Two	33 μH	4.4 μH	80 W	80 W	12480 mm^2
Three	33 μH	4.4 μH	114W	53 W	16898 mm^2
Four	33 μH	4.4 μH	145W	40 W	22626 mm^2

The comparison of the two decoupled transformers is shown in Table II. The leakage inductance for the 12-leg transformer is so small that the operating frequency at the minimum output voltage will be 400 kHz. The total loss of the 8-leg transformer is close to the total loss of the 12-leg core, but the leakage inductance is 52% larger. So, the 8-leg transformer is selected as candidate III at last.

E. Comparison Between the Candidates

This section compares and concludes the previously proposed candidates. The detailed information is shown in Table III.

After comparison, the performance of candidate II is close to separate transformers in terms of inductance, loss, and footprint. Candidate III has 16% more leakage inductance under the same footprint and loss. Candidate IV has 12% smaller total loss under the same leakage inductance and similar footprint. Overall, candidate IV has the smallest total loss with the most leakage inductance integrated among all the four candidates, and is selected for further analysis.

F. Number of Parallel Windings Selection

All the previous sections only discuss the cases with two parallel windings. Since the good current sharing can be realized in a simple way, more parallel windings could also be introduced. This section focuses on selecting the number of parallel windings. The transformers with three parallel windings and four parallel windings are shown in Fig. 16. The transformer information is shown in Table IV. If no parallel windings are introduced, one four-leg transformer is used to handle 22 kW, assuming the core loss is P_{core}, and winding loss is P_w for the transformer. When the number of parallel windings increases,

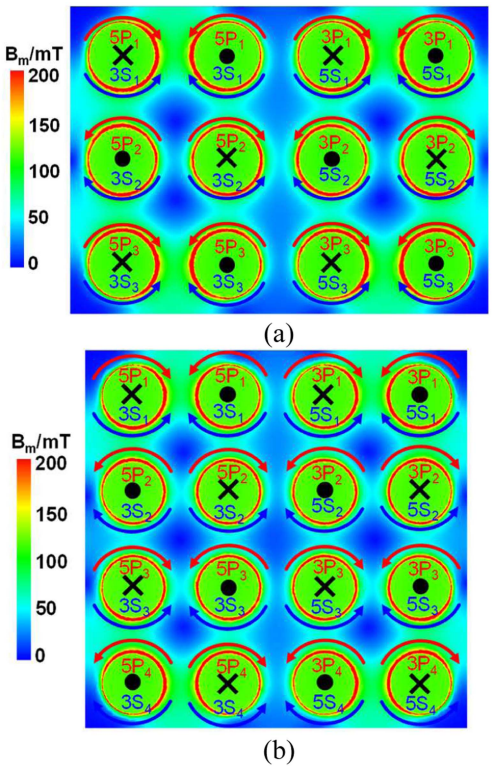

Fig. 16. Decoupled transformer with parallel windings. (a) Three parallel windings. (b) Four parallel windings.

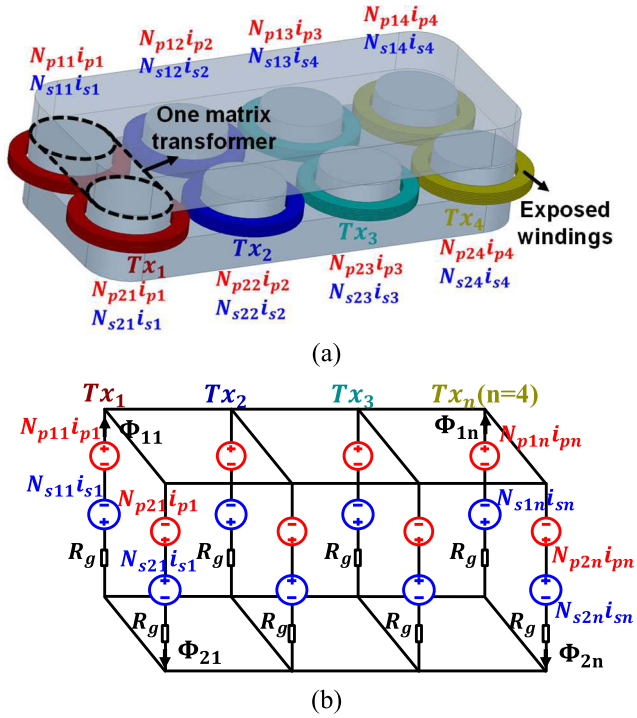

Fig. 17. Proposed scalable high-power transformer. (a) 3-D model of four transformers with independent excitations. (b) Reluctance model of the transformer.

the winding loss decreases, but the core loss increases. The total loss, P_{tot} is calculated in (40), where n is the number of parallel windings. If the reduced winding loss from parallel windings is smaller than the increased core loss, no more parallel windings should be added. Therefore, the most optimized number of parallel windings is realized when the winding loss is close to the core loss, and the optimal number of parallel windings is calculated in (41). Finally, the candidate with two parallel windings is selected for further analysis and optimization because of the smallest total loss and footprint

$$P_{tot} = nP_c + P_w/n^2 \tag{40}$$

$$n_{op} = \sqrt[3]{P_w/P_c}. \tag{41}$$

III. General Analysis and Model of the Proposed High-Power Transformer

The proposed transformer for 22 kW is shown in Fig. 17(a). Some modifications on the core plate are made to the transformer by exposing the windings under the core plate. In this way, the thermal management for the PCB windings will be better, but with a thicker plate and similar core loss. The previous comparison and analysis are only for one specific case. A more general model of the transformer is derived in this chapter, which includes arbitrary numbers of windings around the core legs, excitation directions, and connection patterns. As shown in Fig. 17(a), one matrix transformer is defined with two legs.

The reluctance model of the transformer is shown in Fig. 17(b), identifying the excitations, flux, and key parameters. For the nth transformer, the primary current is defined as i_{pn}, and the secondary current is defined as i_{sn}. Φ_{1n} and Φ_{2n} are the flux flowing through the specified legs. R_g is the reluctance of the air gap. All the following discussions in this chapter will be based on the transformer.

A. Coupling Analysis of the Matrix Transformers

Based on the reluctance model, the MMF on the specified legs can be calculated in (42) and (43). The defined flux flowing through each leg is calculated in (44) and (45). Then, the flux linkage of the nth transformer can be calculated in (46) and (47), indicating that all the matrix transformers are coupled with each other. The inductance matrix will be an 8×8 matrix, as shown in (48) shown at the bottom of the next page, where v_{pn} and $v_{sn}$are the voltages induced on the primary and secondary side winding for the nth transformer, $i_{pn}{}'$ and $i_{sn}{}'$ are the differentials of the current excitations flowing through the primary and secondary side windings with respect to time for the nth transformer. The self-inductances of the primary and secondary side windings for the nth transformer, $L_{p,n}$ and $L_{s,n}$, are calculated in (49) and (50). The mutual inductances between different windings are calculated in (51)–(54), where $M_{pn,sn}$ is the mutual inductance between the primary and secondary windings of the nth transformer, $M_{pn,pm}$ is the mutual inductance between the primary windings of the nth and mth transformer, $M_{pn,sm}$ is the mutual inductance between the primary winding of the nth transformer

and secondary winding of the *m*th transformer, and $M_{sn,sm}$ is the mutual inductance between the secondary windings of the *n*th and *m*th transformer. From the equations, the matrix transformers are coupled with each other, making it hard to design and analyze. So, the matrix transformers need to be decoupled for free connections.

From (51)–(54), the matrix transformers are still coupled if the mutual inductances are not zero. A matrix transformer can be decoupled from the other matrix transformers if (55) is satisfied. The flux inside the matrix transformer, Φ_{tn} is simplified as (56). So, the decoupling requirement is found with a proper physical explanation

$$F_{1n} = N_{p1n}\, i_{pn} - N_{s1n} i_{sn} \tag{42}$$

$$F_{2n} = N_{p2n}\, i_{pn} - N_{s2n} i_{sn} \tag{43}$$

$$\Phi_{1n} = \frac{F_{1n}}{R_g} + 7\sum_{n=1}^{4} \frac{F_{2n} - F_{1n}}{56R_g} \tag{44}$$

$$\Phi_{2n} = \frac{F_{2n}}{R_g} + 7\sum_{n=1}^{4} \frac{F_{1n} - F_{2n}}{56R_g} \tag{45}$$

$$\lambda_{pn} = N_{p1n}\Phi_{1n} + N_{p2n}\Phi_{2n} \tag{46}$$

$$\lambda_{sn} = N_{s1n}\Phi_{1n} + N_{s2n}\Phi_{2n} \tag{47}$$

$$L_{p,n} = \frac{7(N_{p1n}^2 + N_{p2n}^2) + 2N_{p1n}N_{p2n}}{8R_g} \tag{49}$$

$$L_{s,n} = \frac{7(N_{s1n}^2 + N_{s2n}^2) + 2N_{s1n}N_{s2n}}{8R_g} \tag{50}$$

$$M_{pn,sn} = -\frac{7\,(N_{p1n}N_{s1n}+N_{p2n}N_{s2n})+N_{p1n}N_{s2n}+N_{p2n}N_{s1n}}{8R_g} \tag{51}$$

$$M_{pn,pm} = \frac{N_{p1n}(N_{p2m} - N_{p1m}) + N_{p2n}\,(N_{p1m} - N_{p2m})}{8R_g} \tag{52}$$

$$M_{pn,sm} = \frac{N_{p1n}\,(N_{s1m} - N_{s2m}) + N_{p2n}\,(N_{s2m} - N_{s1m})}{8R_g} \tag{53}$$

$$M_{sn,sm} = \frac{N_{s1n}(N_{s1m} - N_{s2m}) + N_{s2n}(N_{s2m} - N_{s1m})}{8R_g} \tag{54}$$

$$N_{p2n} = N_{p1n} = N_{pn};\; N_{s2n} = N_{s1n} = N_{sn} \tag{55}$$

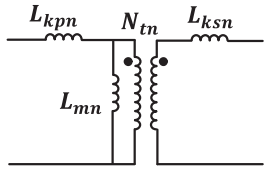

Fig. 18. Transformer T model.

$$\Phi_{tn} = \frac{N_{pn}i_p - N_{sn}i_s}{R_g}. \tag{56}$$

B. Analysis of Transformer Configurations

The previous section analyzes the coupling between the matrix transformers. The impact of different connection patterns on the transformer performance will be introduced in this section.

Fig. 18 shows the general T-model of one single matrix transformer, where N_{tn} is the turns ratio, L_{mn} is the magnetizing inductance, and L_{kpn}, L_{ksn} are the leakage inductances calculated in (57)–(60)

$$N_{tn} = N_{pn}\,/N_{sn} \tag{57}$$

$$L_{mn} = -N_{tn}M_{pn,sn} = 2N_{pn}^2/R_g \tag{58}$$

$$L_{kpn} = L_{pn} - L_{mn} = 0 \tag{59}$$

$$L_{ksn} = L_{sn} - \frac{L_{mn}}{N_{tn}^2} = 0. \tag{60}$$

If all the matrix transformers are connected in series, the turns ratio, magnetizing inductance, and leakage inductances can be calculated using the T-model in (61)–(64). From the equations, the leakage inductance is mainly introduced by the difference of the primary and secondary turns numbers. The same calculation process can be applied to circumstances with more matrix transformers integrated. So, the series connection could introduce leakage inductance and reduce the volt-second at high voltage applications based on Faraday's law

$$N_t = \frac{\sum_{n=1}^{4} N_{pn}}{\sum_{n=1}^{4} N_{sn}} \tag{61}$$

$$L_m = \frac{\sum_{n=1}^{4} N_{pn}}{\sum_{n=1}^{4} N_{sn}} \cdot \sum_{n=1}^{4} \frac{2N_{pn}N_{sn}}{R_g} \tag{62}$$

$$L_{kp} = \sum_{n=1}^{4} \frac{4N_{pn}^2}{R_g} - \frac{\sum_{n=1}^{4} N_{pn}}{\sum_{n=1}^{4} N_{sn}} \cdot \sum_{n=1}^{4} \frac{2N_{pn}N_{sn}}{R_g} \tag{63}$$

$$\begin{bmatrix} v_{p1} \\ v_{s1} \\ v_{p2} \\ v_{s2} \\ v_{p3} \\ v_{s3} \\ v_{p4} \\ v_{s4} \end{bmatrix} = s \begin{bmatrix} L_{p,1} & M_{p1,s1} & M_{p1,p2} & M_{p1,s2} & M_{p1,p3} & M_{p1,s3} & M_{p1,p4} & M_{p1,s4} \\ M_{p1,s1} & L_{s,1} & M_{p2,s1} & M_{s1,s2} & M_{p3,s1} & M_{s1,s3} & M_{p4,s1} & M_{s1,s4} \\ M_{p1,p2} & M_{p2,s1} & L_{p,2} & M_{p2,s2} & M_{p2,p3} & M_{p2,s3} & M_{p2,p4} & M_{p2,s4} \\ M_{p1,s2} & M_{s2,s1} & M_{p2,s2} & L_{s,2} & M_{p3,s2} & M_{s2,s3} & M_{p4,s2} & M_{s2,s4} \\ M_{p1,p3} & M_{p3,s1} & M_{p2,p3} & M_{p3,s2} & L_{p,3} & M_{p3,s3} & M_{p3,p4} & M_{p3,s4} \\ M_{p1,s3} & M_{s3,s1} & M_{p2,s3} & M_{s2,s3} & M_{p3,s3} & L_{s,3} & M_{p4,s3} & M_{s3,s4} \\ M_{p1,p4} & M_{p4,s1} & M_{p2,p4} & M_{p4,s2} & M_{p3,p4} & M_{p4,s3} & L_{p,4} & M_{p4,s4} \\ M_{p1,s4} & M_{s4,s1} & M_{p2,s4} & M_{s2,s4} & M_{p3,s4} & M_{s3,s4} & M_{p4,s4} & L_{s,4} \end{bmatrix} \begin{bmatrix} i'_{p1} \\ i'_{s1} \\ i'_{p2} \\ i'_{s2} \\ i'_{p3} \\ i'_{s3} \\ i'_{p4} \\ i'_{s4} \end{bmatrix} \tag{48}$$

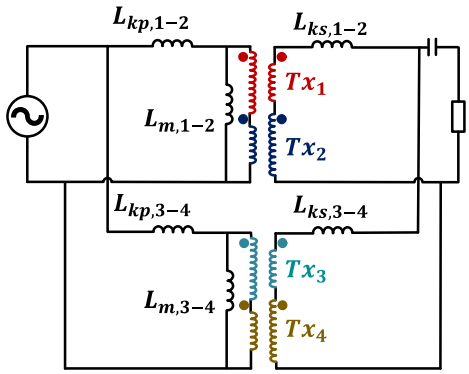

Fig. 19. Transformer with hybrid connection.

$$L_{ks} = \sum_{n=1}^{4} \frac{4N_{sn}^2}{R_g} - \frac{\sum_{n=1}^{4} N_{sn}}{\sum_{n=1}^{4} N_{pn}} \cdot \sum_{n=1}^{4} \frac{2N_{pn}N_{sn}}{R_g}. \quad (64)$$

Parallel connections are adopted to reduce the current stress on the PCB windings. Based on the previous analysis, the current distribution is mainly impacted by the leakage inductance, controlled by the turns number and air gap. Therefore, the hybrid connection is proposed. The circuit diagram of the hybrid connection is shown in Fig. 19. Tx_1 and Tx_2 are connected in series, and Tx_3 and Tx_4 are connected in series. Then, the windings are connected in parallel. Good current sharing can be realized if (65) can be realized by controlling the turns numbers

$$\begin{aligned} L_{kp,1-2} &= L_{kp,3-4} \\ L_{ks,1-2} &= L_{ks,3-4}. \end{aligned} \quad (65)$$

C. Matrix Transformers Arrangement and Flux Distributions

Since all the transformers are decoupled, the matrix transformers can be freely arranged. The arrangements do not impact the flux in the core legs or the inductances but affect the flux distribution on the core plates. To analyze the flux distribution on the plate, the total flux is separated into two components as calculated in (66). One is the triangular waveform generated by the magnetizing current; the other is the sinusoidal waveform generated by the load current.

$$\Phi_{tn} = \frac{N_{pn} i_m}{R_g} + \frac{(N_{pn} - N_{sn})\, i_s}{R_g}. \quad (66)$$

The plate flux distribution is impacted by the MMF and the reluctance on the core. Therefore, different arrangements have different flux distributions on the plate. An arrangement satisfying (65) is shown in Fig. 20(a), where R_c is the core reluctance, much smaller than R_g. The blue and red arrows indicate the winding directions around the core legs. The white dots and crosses show the direction of the magnetizing flux, which are triangular waveforms. Based on the reluctance model, the flux through all the paths could be analyzed. The flux is shown in Fig. 20(b), calculated based on (33). According to the figure, path two (P2) and path three (P3) only have triangular flux going through. P4 only has sinusoidal flux going through. P1 has both kinds of flux going through. Fig. 20(a) shows the maximum flux density of the transformer. Based on the simulation, the core loss for case I is 99 W at the nominal condition. From the analysis, the flux is not evenly distributed, especially the sinusoidal flux.

TABLE V
TRANSFORMER ARRANGEMENT COMPARISON

Arrangement	Core loss	Winding loss	Footprint
I	99 W	80 W	12480 mm^2
II	80 W	80 W	12480 mm^2
III	85 W	80 W	12480 mm^2
IV	102 W	80 W	12480 mm^2

To have the best flux distribution, the flux in one leg consistently opposes the flux in all surrounding legs, as shown in Fig. 21(a). In this arrangement, the horizontal reluctance and vertical reluctance are the same for both kinds of legs. More evenly distributed flux is realized. The calculated flux distribution is shown in Fig. 21(b). P2 and P3 now have sinusoidal flux. Both the flux through P1 and P4 are reduced. The maximum flux is reduced by 20 μWb compared to arrangement I. The core loss for case II is 80 W, a 20% reduction.

Although arrangement II can realize the lowest core loss, the winding inlets and outlets are on the short edge for PCB layout, which is better suited for narrow PCB layouts. However, the transformer will fit into the final hardware better in this work. Therefore, arrangement III is proposed with winding inlets and outlets on the long edge is shown in Fig. 22(a). The flux distribution is calculated in Fig. 22(b).

Table V shows the information on the cases discussed. Arrangement IV uses two separate four-leg transformers with the same winding patterns shown in Fig. 23, assuming good current sharing is realized for both transformers. Compared to separate cores, the best structure has a 22% core loss reduction. Considering loss and layout, arrangement III is selected at last.

IV. CLLC Resonant Converter Design Steps and Considerations

This paragraph discusses the design steps and considerations of the CLLC resonant converter, including topology comparison and transformer parameter selection. The design flowchart is shown in Fig. 24.

A. Transformer Parameter Design

This section focuses on the transformer parameters design, including magnetizing inductance L_m, turns ratio n, and leakage inductance L_k.

First, the device loss for different dead time, t_d is swept as shown in Fig. 25. To achieve zero voltage switching (ZVS), the magnetizing inductance should satisfy (67), where T_s is the switching period, t_d is the dead time, C_{oss} is the output capacitance of the device, and n is the turns ratio. Small magnetizing inductance means larger magnetizing current and more device loss, so the boundary of inductance values are chosen for different dead time. The total device loss includes the conduction

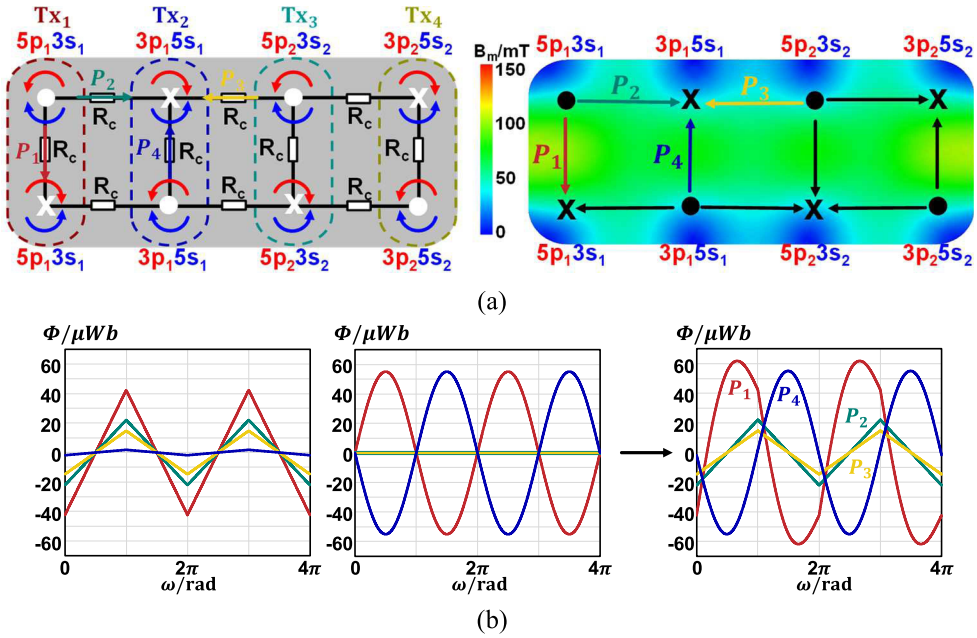

Fig. 20. Arrangement I: (a) winding arrangement and core flux distribution; (b) calculated flux on the core plates.

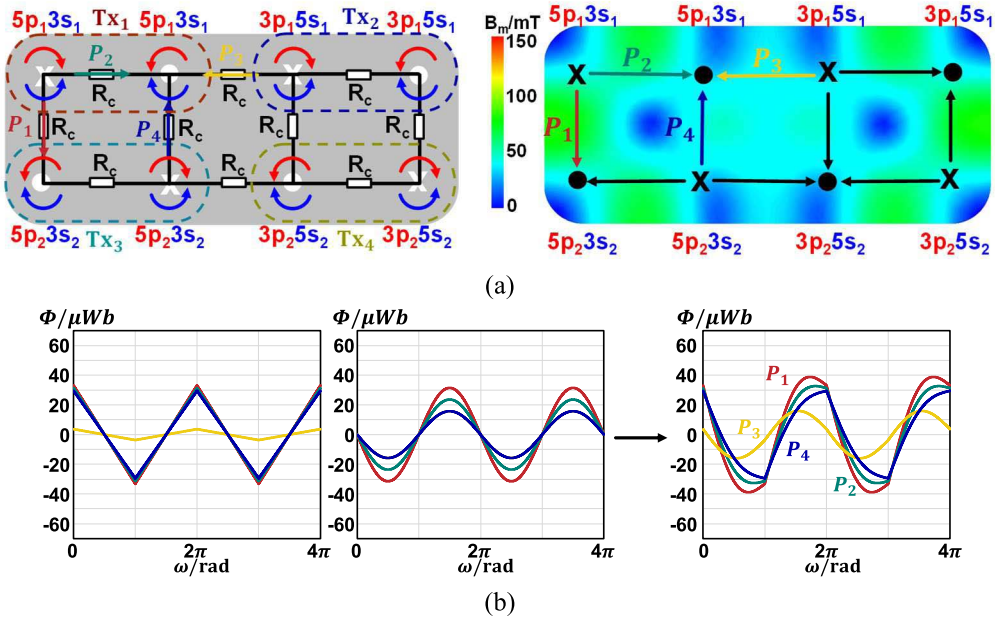

Fig. 21. Arrangement II: (a) winding arrangement and core flux distribution; (b) calculated flux on the core plates.

loss for the primary and the secondary devices calculated in (68), the primary turnoff loss calculated in (69), and the driving loss calculated in (70), where N_Q and N_{SR} are the number of primary and secondary side devices, I_{rms_Q} and I_{rms_SR} are the RMS current flowing through the primary and secondary devices, $R_{ds\_on\_Q}$ and $R_{ds\_on\_SR}$ are the drain-to-source on resistance of the primary and secondary devices, E_{off} is the turn off energy, f_{sw} is the switching frequency, V_{f_Q} and V_{f_SR} are the gate voltage amplitude for the primary and secondary devices, Q_{g_Q} and Q_{g_SR} are the total gate charge of the primary and secondary devices. At last, t_d is selected to be 130 ns for the lowest device loss, and L_m is selected to be 33 μH for ZVS

$$L_m \le \frac{\left(\frac{T_s}{2} - t_d\right) t_d}{16 C_{oss}\left(1 + 1/n^2\right)} \tag{67}$$

$$P_{cond} = N_Q\, I_{rms\_Q}^2 R_{ds\_on\_Q} + N_{SR} I_{rms\_SR}^2 R_{ds\_on\_SR} \tag{68}$$

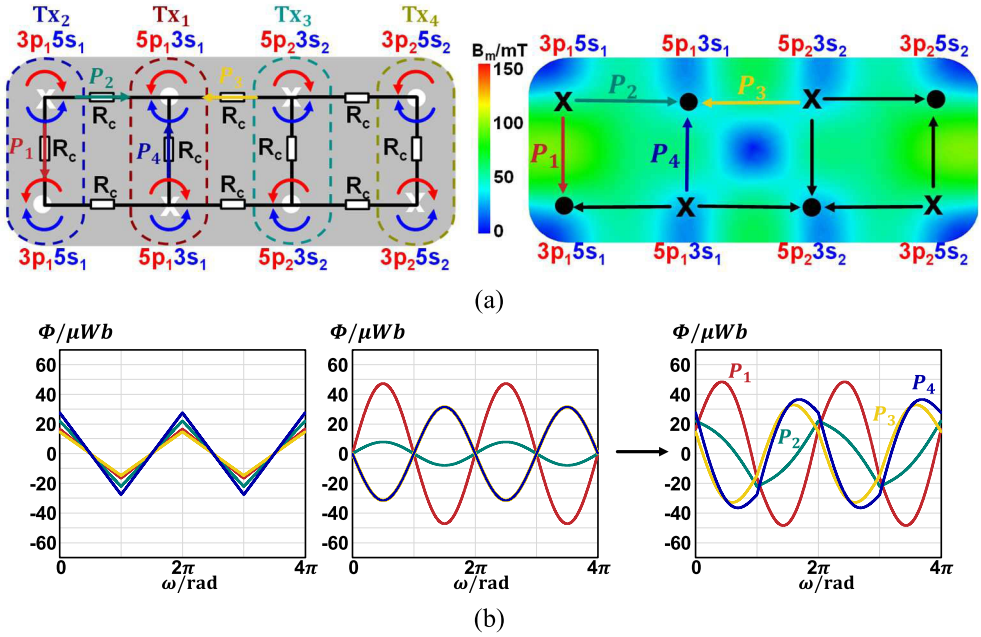

Fig. 22. Arrangement III: (a) winding arrangement and core flux distribution; (b) calculated flux on the core plates.

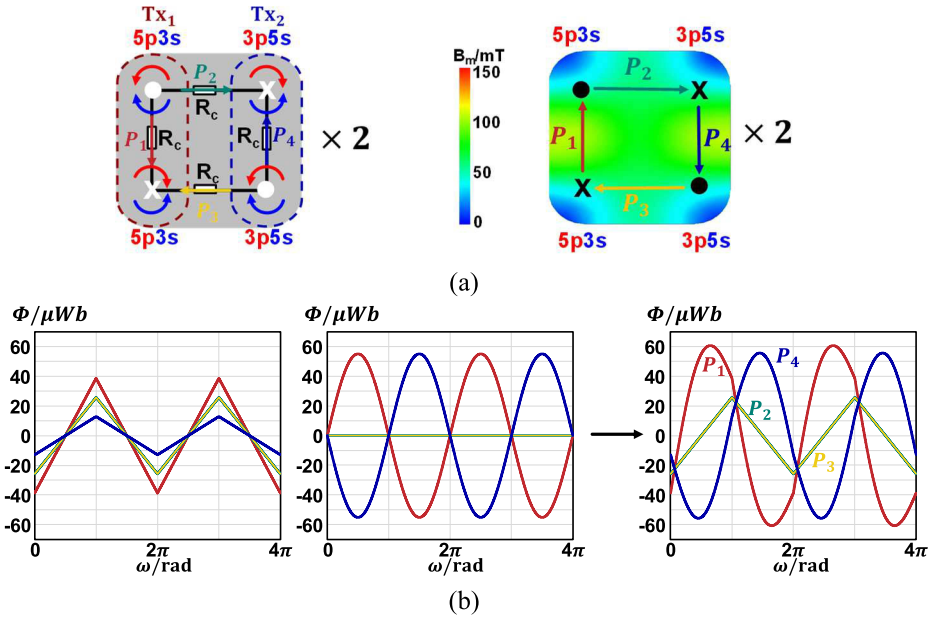

Fig. 23. Arrangement IV: (a) winding arrangement and core flux distribution; (b) calculated flux on the core plates.

$$P_{turn\_off} = N_Q \, E_{off} f_{sw} \tag{69}$$

$$P_{dri} = N_Q \, V_{f\_Q} Q_{g\_Q} f_{sw} + N_{SR} V_{f\_SR} Q_{g\_SR} f_{sw} \tag{70}$$

$$L_n = L_m \frac{}{L_r}. \tag{71}$$

Then, the operating frequency range for different possible turns numbers and L_n defined in (71) are compared as shown in Table VI using eight layers PCB. From the table, the frequency range is minimized when the turns ratio is equal to one. For larger L_n, the maximum switching frequency is 400 kHz, dramatically

TABLE VI
FREQUENCY RANGE FOR DIFFERENT PARAMETERS

Turns ratio	L_n	f_{min}/kHz	f_{max}/kHz
8:8	3	250	285
8:7	3	180	265
8:8	7.5	250	338
8:7	7.5	175	293
8:8	11.5	250	400
8:7	11.5	155	320

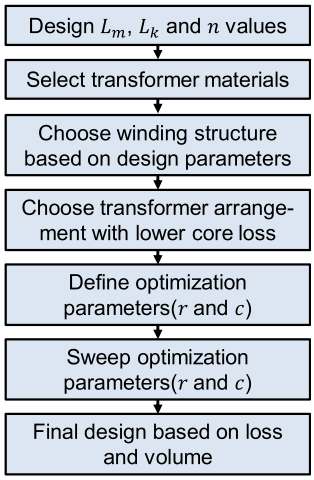

Fig. 24. Design steps of the proposed transformer.

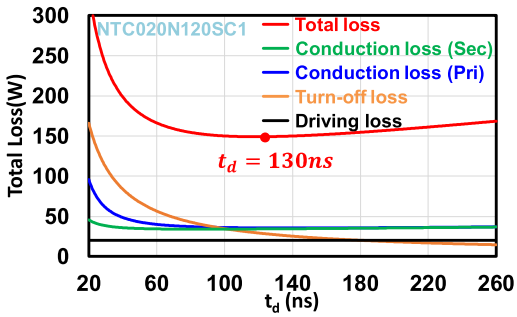

Fig. 25. Device loss versus dead time at the nominal condition.

TABLE VII
RESONANT TANK PARAMETERS

Parameters	Value	Parameters	Value
Turns ratio (n)	1	L_k/μH	4.4
L_m/μH	33	C_r/nF	92

increasing the loss at the lowest output voltage. For smaller L_n, the interleaving of the transformer windings is sacrificed. So, both winding land core losses are increased, lowering the peak efficiency. When L_n equals 7.5, the maximum frequency is below 350 kHz, and the transformer loss is acceptable. So, L_n is selected to be 7.5 at last. The final resonant tank parameters are shown in Table VII.

B. Transformer Materials Selection and Optimization Parameters Definition

This section selects the core material, and winding thickness, and defines the parameters that must be optimized.

The core loss density versus the maximum flux density at the resonant frequency is shown in Fig. 26. DMR96A was chosen because of the smaller core loss density. The skin depth of copper at 250 kHz is about 130 μm, so 4 oz copper is selected, whose thickness is around 139 μm.

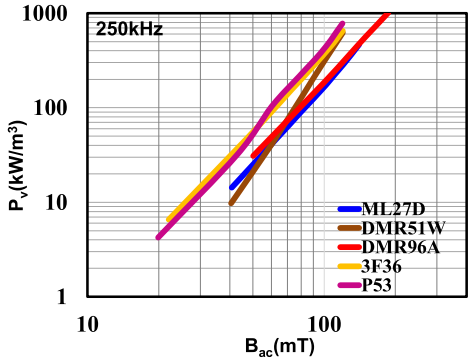

Fig. 26. Core loss density of different materials at 250 kHz.

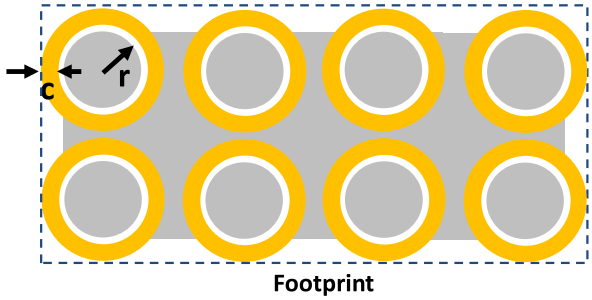

Fig. 27. Transformer optimization parameters definition.

The transformer optimization parameters are defined in Fig. 27, including the core radius r and winding width c. The optimization process will be the tradeoff between the transformer footprint and the total loss. Different r and c combinations will also impact the distribution of core loss and winding loss.

C. Transformer Optimization Process

After defining the optimization parameters, this part shows the optimization process based on the nominal condition at 22 kW 750 V input voltage.

finite element analysis (FEA) simulations are run for different r and c combinations. The core loss is obtained from the 3-D simulations, including hysteresis loss and eddy current loss [20]. The winding loss is obtained from the 2-D simulations because of the finer mesh. The results are shown in Fig. 28. When the core radius increases, core loss will decrease with a larger cross-sectional area, and winding loss will increase with more extended windings. When the winding width increases, the winding loss will decrease with a smaller current density, and core loss only increases slightly because of the limited impact on the total core volume.

Fig. 28(c) shows the plot of the total loss of the transformer. The dashed lines represent transformers with the same footprint. Each dashed line is tangent to a curve with the same total loss. The intersection point means the transformer with the smallest loss under the same footprint. If all the intersection points are collected, Fig. 29 can be obtained with the optimal cases. The total transformer loss tends to be flat when the footprint is close to 13000 mm^2.

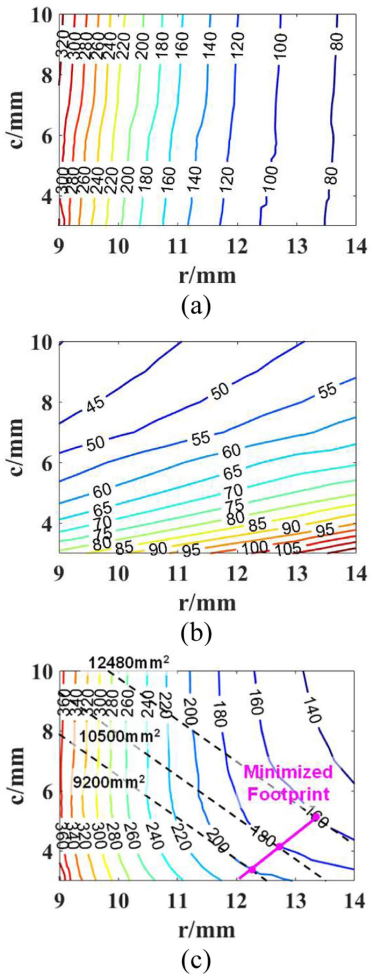

Fig. 28. Loss information for different r and c combinations: (a) core loss; (b) winding loss; and (c) total loss.

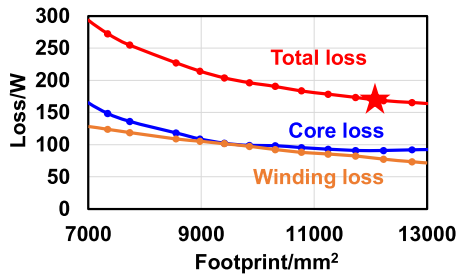

Fig. 29. Detailed loss distribution of the optimal design points.

Considering the PCB layout, the final footprint is selected to be 12480 mm^2. The final transformer parameters are shown in Table VIII.

V. Experimental Results

A. Converter Prototype

The prototype is shown in Fig. 30. The details are shown in Table IX.

TABLE VIII
Transformer Details

Parameters	Value
Core material	DMR96A
PCB winding thickness	4 oz
Core radius, r	13.5 mm
Winding width, c	5 mm
Footprint	12480 mm^2

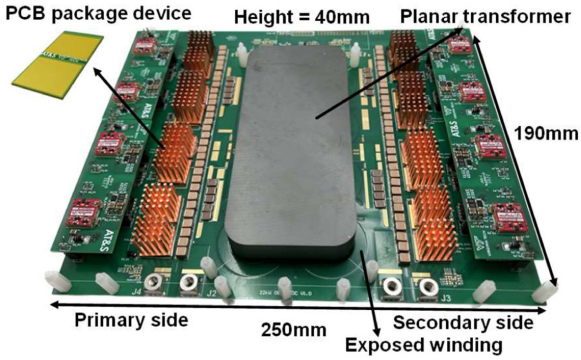

Fig. 30. 22-kW CLLC resonant converter prototype.

TABLE IX
Prototype Details

Parameters	Value
Input voltage, V_{in}	650 V– 850 V
Output voltage, V_o	550 V– 850 V
Maximum output power, $P_{\max}$	22 kW
Resonant frequency	250 kHz
Maximum output current, $I_{\max}$	30 A
Magnetizing inductance, L_m	33.6 µH
Leakage inductance, $L_{kp} = L_{ks}$	4.6 µH
Resonant capacitance, $C_{rp} = C_{rs}$	90 nF
Devices' part number	NTC020N120SC1
Gate Driver	UCC 21750
Mainboard PCB	4 layers 4 oz
Daughter board PCB	4 layers 4 oz
Prototype dimensions	250 × 190 × 40 mm
Power density	11.6 kW/L

The devices are commercial dies packaged into the PCB by AT&S [19]. The L_n value in the real transformer is 7.3, which is only 2.6% away from the calculation result of 7.5. The main power stage uses a 4-layer, 4-oz PCB. Another 4-layer, 4-oz PCB daughter board is connected to the bottom only for the PCB windings.

B. Experimental Testing Results

Figs. 31 and 32 show the tested results at different conditions. V_{ds_Q2} and V_{gs_Q2} are the drain to source voltage and the gate voltage for the primary low side switch. I_{p_1} and I_{p_2} are the currents flowing through the parallel primary side windings,

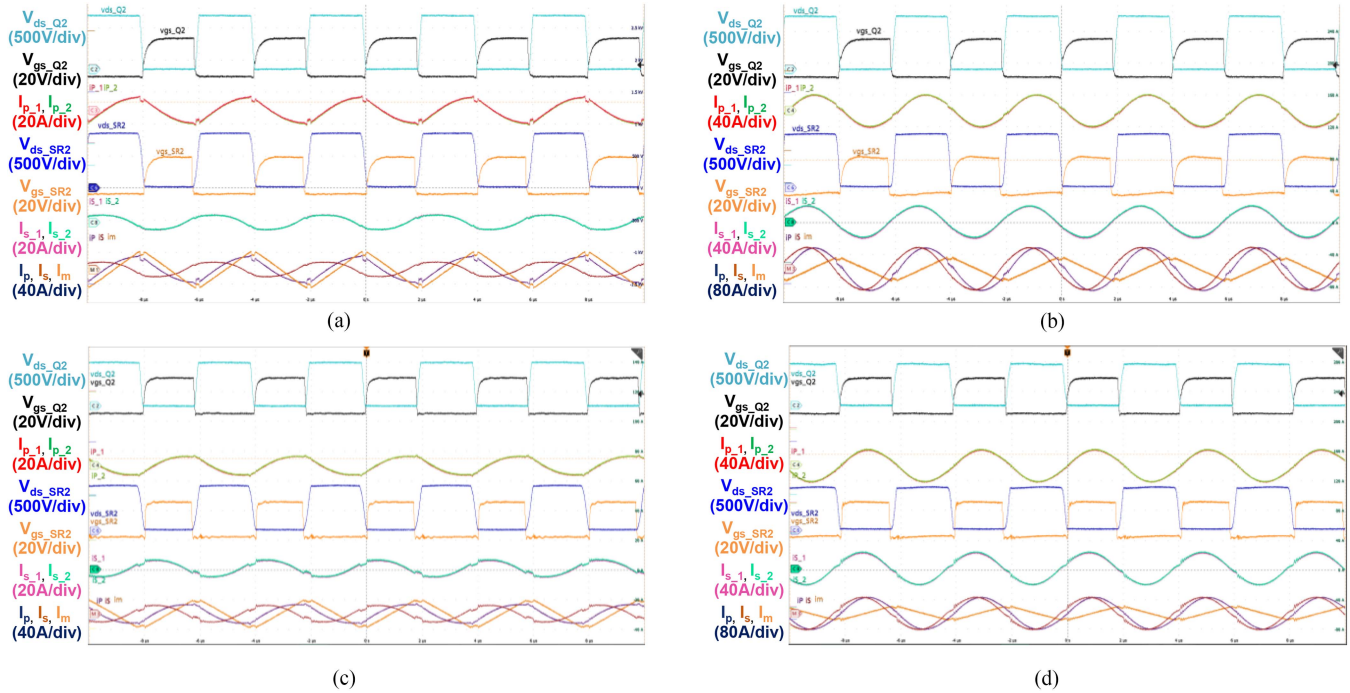

Fig. 31. Testing waveforms at different conditions. (a) $V_{in} = V_o$ =850 V, P_o = 4.4 kW; (b) $V_{in} = V_o$ =850 V, P_o = 22 kW; (c) $V_{in} = V_o$ = 750 V, P_o = 4.4 kW; (d) $V_{in} = V_o$ = 750 V, P_o = 22 kW.

TABLE X
PERFORMANCE COMPARISON

Parameter	[1]	[2]	[3]	[4]	[5]	[6]	This work
Input voltage / V	550 – 840	800	380 – 660	550 – 850	650 – 900	400	650 – 850
Output voltage / V	250 – 450	150 – 950	200 – 500	450 – 850	200 – 800	100–395	550 – 850
Max. power / kW	6.6	6.6	6.6	11	22	22	22
Resonant Freq. / kHz	500	500	300	250	200	100	250
Peak efficiency	97.8%	98.2%	98.1%	98.4%	98.5%	~97%	98.5%
Power density / kW/L	8	7.3	N/A	15.2	8	3	11.6
Magnetic Components	2	3	2	1	4	12	1

respectively. V_{ds_SR2} and V_{gs_SR2} are the drain to source voltage and the gate voltage for the secondary low side switch. I_{s_1} and I_{s_2} are the currents flowing through the parallel secondary side windings, respectively, I_p, I_s, and I_m are the total primary side current, total secondary side current, and the magnetizing current, respectively.

The current is more triangular at the light load from the waveforms because magnetizing current takes the majority. When the load increases, the waveform becomes a sinusoidal waveform because the load current takes the majority. Perfect current sharing is realized under all the conditions.

The converter efficiency at different load conditions is shown in Fig. 33. The full load power is 22 kW. The efficiency at different output voltages is shown in Fig. 34. Fig. 35 shows the loss decomposition at the nominal condition.

Magnetic loss and device loss take a larger composition. The other loss includes the loss on vias, ESR loss of the resonant capacitors and decoupling capacitors, and loss on the PCB traces.

The maximum current limit is 30 A in the charging profile. The peak efficiency is 98.5%. The highest full load efficiency is 98.4%.

Fig. 36 shows the thermal performance at 550 V, 16.5 kW at the worst case after 10 min. The ambient temperature is 25 °C. The maximum winding temperature is 80 °C. The maximum core temperature is 55 °C. The thermal distribution on the core plate matches the flux distribution analysis well. Since the PCB windings are exposed, the thermal performance could be better with a customized cold plate. The comparison between this work and the other works is shown in Table X.

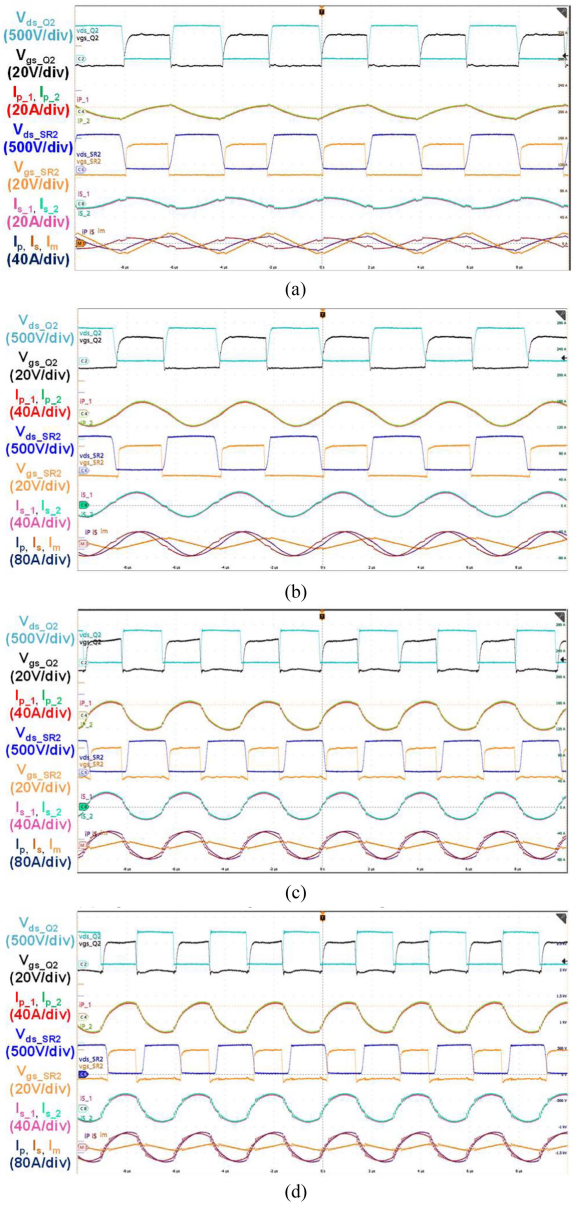

Fig. 32. Testing waveforms at different conditions. (a) $V_{in} = V_o = 650$ V, $P_o = 4.4$ kW; (b) $V_{in} = V_o = 650$ V, $P_o = 19.8$ kW; (c) $V_o = 650$ V, $V_o = 600$ V, $P_o = 18$ kW; (d) $V_o = 650$ V, V_o =550 V, $P_o = 16.5$ kW.

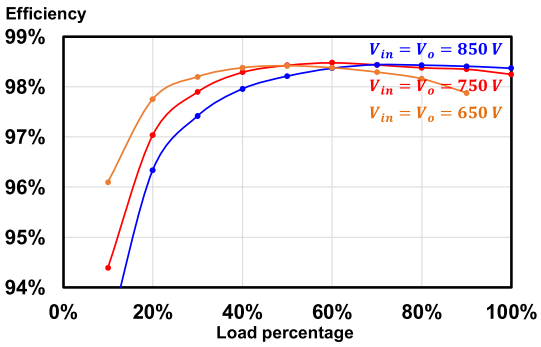

Fig. 33. Converter efficiency under different load conditions ($P_{o\_\max}$ = 22 kW).

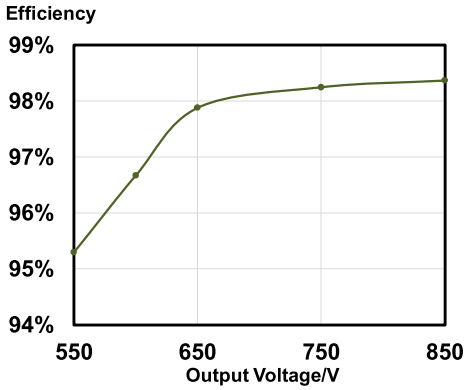

Fig. 34. Converter efficiency for different output voltage in the charging profile ($I_{o\_max} = 30$ A).

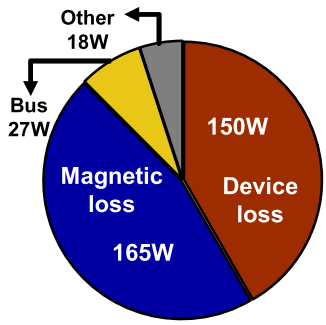

Fig. 35. Loss decomposition at the nominal condition ($V_{in} = V_o = 750$ V, $P_o = 22$ kW).

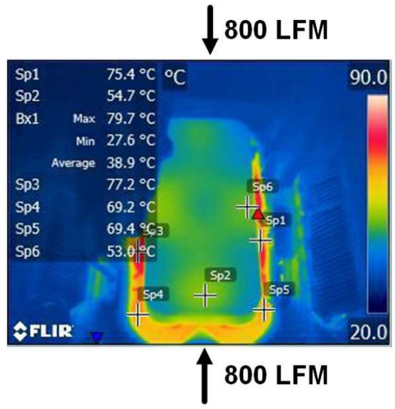

Fig. 36. Thermal performance at the worst case ($V_o = 550$ V, $P_o = 16.5$ kW, 10 min).

VI. Conclusion

This article proposes a 22-kW planar transformer design with a detailed analysis of the coupling behavior, current, and flux distributions. The excitations on the core legs are found to impact the coupling of the parallel windings. The parallel windings can have positive coupling, negative coupling, and decoupling behaviors with different excitations. Different numbers of parallel windings are also compared.

A way to decouple the matrix transformers without decoupling legs is proposed to expose the windings for better thermal performance. The perfect current sharing is realized under all the conditions. The transformer also has good scalability because of the good current sharing. The analyzed and most optimized matrix transformers' arrangement has a 22% smaller core loss than two separated transformers.

Because of the integrated planar transformer and the optimization process, the 22-kW CLLC resonant converter prototype could reach 98.5% peak efficiency and 11.6 kW/L power density.

Acknowledgment

The authors would like to thank Dr. Christina DiMarino of Virginia Tech, Mr. Hannes Stahr, and Mr. Mike Morianz of AT&S for their valuable and constructive suggestions during the development of this research work.

This work was conducted with the PCB packaged devices produced by AT&S and the core samples donated in kind by DMEGC.

Appendix I
Inductance Calculations for Candidate II

The detailed inductance calculations are derived in this appendix for candidate II with negative coupling. The reluctance model is shown in Fig. 7. The MMFs generated by the windings in different legs are calculated in (A1)–(A4) as F_{aleg1} - F_{dleg3}, where i_{p1}, i_{p2} are the current excitations for the primary two parallel windings, i_{s1}, i_{s2} are the current excitations for the secondary two parallel windings

$$F_{aleg1} = F_{aleg2} = F_{aleg3} = 5i_{p1} - 3i_{s1} \tag{A1}$$

$$F_{bleg1} = F_{bleg2} = F_{bleg3} = 3i_{p1} - 5i_{s1} \tag{A2}$$

$$F_{cleg1} = F_{cleg2} = F_{cleg3} = 5i_{p2} - 3i_{s2} \tag{A3}$$

$$F_{dleg1} = F_{dleg2} = F_{dleg3} = 3i_{p2} - 5i_{s2}. \tag{A4}$$

The next step is to calculate the flux in each leg. Unlike the proposed decoupled case, the calculations for the coupled transformers are more complicated because the flux from the other legs needs to be considered. The flux in each leg is calculated in (A5)–(A12), with directions shown in Fig. 7. R_g is the reluctance of the air gap

$$\Phi_{aleg1} = \Phi_{aleg3} = \frac{29}{6R_g}\, i_{p1} - \frac{19}{6R_g} i_{s1} - \frac{1}{6R_g}\,(i_{p2} + i_{s2}) \tag{A5}$$

$$\Phi_{aleg2} = \Phi_{aleg2} = \frac{31}{6R_g}\, i_{p1} - \frac{17}{6R_g} i_{s1} + \frac{1}{6R_g}\,(i_{p2} + i_{s2}) \tag{A6}$$

$$\Phi_{bleg1} = \Phi_{bleg3} = \frac{29}{6R_g}\, i_{s1} - \frac{19}{6R_g} i_{p1} - \frac{1}{6R_g}\,(i_{p2} + i_{s2}) \tag{A7}$$

$$\Phi_{bleg2} = \frac{31}{6R_g}\, i_{s1} - \frac{17}{6R_g} i_{p1} + \frac{1}{6R_g}\,(i_{p2} + i_{s2}) \tag{A8}$$

$$\Phi_{cleg1} = \Phi_{cleg3} = \frac{29}{6R_g}\, i_{p2} - \frac{19}{6R_g} i_{s2} - \frac{1}{6R_g}\,(i_{p1} + i_{s1}) \tag{A9}$$

$$\Phi_{cleg2} = \frac{31}{6R_g}\, i_{p2} - \frac{17}{6R_g} i_{s2} + \frac{1}{6R_g}\,(i_{p1} + i_{s1}) \tag{A10}$$

$$\Phi_{dleg1} = \Phi_{dleg3} = \frac{29}{6R_g}\, i_{s2} - \frac{19}{6R_g} i_{p2} - \frac{1}{6R_g}\,(i_{p1} + i_{s1}) \tag{A11}$$

$$\Phi_{dleg2} = \frac{31}{6R_g}\, i_{s2} - \frac{17}{6R_g} i_{p2} + \frac{1}{6R_g}\,(i_{p2} + i_{s2})\,. \tag{A12}$$

Based on Faraday's law shown in (A13), the total voltage of each winding is the summation of the voltage induced on each leg

$$v = N \cdot \frac{d\Phi}{dt}. \tag{A13}$$

Then we can get the inductance matrix calculated in (A14), where v_{p1}, v_{p2} are the voltage induced on the two primary parallel windings, v_{s1}, v_{s2} are the voltage induced on the two secondary parallel windings

$$\begin{bmatrix} v_{p1} \\ v_{s1} \\ v_{p2} \\ v_{s2} \end{bmatrix} = \begin{bmatrix} \frac{305}{3R_g} & -\frac{271}{3R_g} & -\frac{1}{3R_g} & -\frac{1}{3R_g} \\ -\frac{271}{3R_g} & \frac{305}{3R_g} & -\frac{1}{3R_g} & -\frac{1}{3R_g} \\ -\frac{1}{3R_g} & -\frac{1}{3R_g} & \frac{305}{3R_g} & -\frac{271}{3R_g} \\ -\frac{1}{3R_g} & -\frac{1}{3R_g} & -\frac{271}{3R_g} & \frac{305}{3R_g} \end{bmatrix} \begin{bmatrix} i_{p1}{}' \\ i_{s1}{}' \\ i_{p2}{}' \\ i_{s2}{}' \end{bmatrix}. \tag{A14}$$

Since parallel windings are introduced to the transformer, (A15) and (A16) is met if the transformer is seen as a whole, where v_p, v_s are the total voltage across the primary and secondary windings, i_p, i_s are the total current excitations for the primary and secondary windings. Then (A14) can be transformed into (A17), with the self-inductance and the mutual inductance. From the T model shown in Fig. 18, the magnetizing inductance and leakage inductance can be calculated in (A18) and (A19)

$$v_p = v_{p1} = v_{p2}\ ;\ \ v_s = v_{s1} = v_{s2} \tag{A15}$$

$$i_p = i_{p1} + i_{p2};\ \ i_s = i_{s1} + i_{s2} \tag{A16}$$

$$\begin{bmatrix} v_p \\ v_s \end{bmatrix} = \begin{bmatrix} \frac{152}{3R_g} & -\frac{136}{3R_g} \\ -\frac{136}{3R_g} & \frac{152}{3R_g} \end{bmatrix} \begin{bmatrix} i_p \\ i_s \end{bmatrix} \tag{A17}$$

$$L_m = \frac{136}{3R_g} \tag{A18}$$

$$L_{kp} = L_{ks} = \frac{16}{3R_g}. \tag{A19}$$

References

[1] B. Li, Q. Li, F. C. Lee, Z. Liu, and Y. Yang, "A high-efficiency high-density wide-bandgap device-based bidirectional on-board charger," *IEEE J. Emerg. Sel. Topics Power Electron.*, vol. 6, no. 3, pp. 1627–1636, Sep. 2018, doi: 10.1109/JESTPE.2018.2845846.

[2] S. Mukherjee, J. M. Ruiz, and P. Barbosa, "A high power density wide range DC–DC converter for universal electric vehicle charging," *IEEE Trans. Power Electron.*, vol. 38, no. 2, pp. 1998–2012, Feb. 2023, doi: 10.1109/TPEL.2022.3217092.

[3] H. Li et al., "A bidirectional synchronous/asynchronous rectifier control for wide battery voltage range in SiC bidirectional LLC chargers," *IEEE Trans. Power Electron.*, vol. 37, no. 5, pp. 6090–6101, May 2022, doi: 10.1109/TPEL.2021.3126886.

[4] F. Jin, A. Nabih, Z. Li, and Q. Li, "A scalable matrix integrated transformer with controllable leakage inductance for a bi-directional resonant converter," *IEEE Trans. Power Electron.*, vol. 38, no. 9, pp. 10967–10984, Sep. 2023, doi: 10.1109/TPEL.2023.3270400.

[5] C. Wei, D. Zhu, H. Xie, Y. Liu, and J. Shao, "A SiC-based 22kW Bidirectional CLLC resonant converter with flexible voltage gain control scheme for EV on-board charger," in *Proc. PCIM Eur. Digit. Days, Int. Exhib. Conf. Power Electron., Intell. Motion, Renewable Energy Energy Manage.*, 2020, pp. 1–7.

[6] J. Schmenger, S. Endres, S. Zeltner, and M. März, "A 22 kW on-board charger for automotive applications based on a modular design," in *Proc. IEEE Conf. Energy Convers.*, 2014, pp. 1–6. doi: 10.1109/CENCON.2014.6967467.

[7] T. Yuan, F. Jin, Z. Li, and Q. Li, "Current sharing analysis of a high power transformer with parallel windings," in *Proc. IEEE Appl. Power Electron. Conf. Expo.*, 2023, pp. 1551–1556. doi: 10.1109/APEC43580.2023.10131421.

[8] W. Chen, Y. Yan, Y. Hu, and Q. Lu, "Model and design of PCB parallel winding for planar transformer," *IEEE Trans. Magn.*, vol. 39, no. 5, pp. 3202–3204, Sep. 2003, doi: 10.1109/TMAG.2003.816147.

[9] M. Chen, M. Araghchini, K. K. Afridi, J. H. Lang, C. R. Sullivan, and D. J. Perreault, "A systematic approach to modeling impedances and current distribution in planar magnetics," *IEEE Trans. Power Electron.*, vol. 31, no. 1, pp. 560–580, Jan. 2016, doi: 10.1109/TPEL.2015.2411618.

[10] M. Li, Z. Ouyang, and M. A. E. Andersen, "Discovery of the nearly zero flux between two parallel conductors in planar transformers," *IEEE Trans. Power Electron.*, vol. 37, no. 1, pp. 714–723, Jan. 2022, doi: 10.1109/TPEL.2021.3093171.

[11] R. Yu, T. Chen, P. Liu, and A. Q. Huang, "A 3-D winding structure for planar transformers and its applications to LLC resonant converters," *IEEE J. Emerg. Sel. Topics Power Electron.*, vol. 9, no. 5, pp. 6232–6247, Oct. 2021, doi: 10.1109/JESTPE.2021.3052712.

[12] Y. Cao, M. Ngo, N. Yan, D. Dong, R. Burgos, and A. Ismail, "Design and implementation of an 18-kW 500-kHz 98.8% efficiency high-density battery charger with partial power processing," *IEEE J. Emerg. Sel. Topics Power Electron.*, vol. 10, no. 6, pp. 7963–7975, Dec. 2022, doi: 10.1109/JESTPE.2021.3108717.

[13] Y. Cao, K. Ngo, and D. Dong, "A scalable electronic-embedded transformer, a new concept toward ultra-high-frequency high-power transformer in DC–DC converters," *IEEE Trans. Power Electron.*, vol. 38, no. 8, pp. 9278–9293, Aug. 2023, doi: 10.1109/TPEL.2023.3279259.

[14] T. Yuan, F. Jin, Z. Li, C. Zhao, and Q. Li, "Design of an integrated transformer with parallel windings for a 30-kW LLC resonant converter," *IEEE Trans. Power Electron.*, vol. 38, no. 11, pp. 14317–14333, Nov. 2023, doi: 10.1109/TPEL.2023.3291954.

[15] T. Yuan, F. Jin, Z. Li, and Q. Li, "High frequency high power integrated transformer design for resonant converters with SiC devices," in *Proc. IEEE 9th Workshop Wide Bandgap Power Devices Appl.*, 2022, pp. 170–175. doi: 10.1109/WiPDA56483.2022.9955265.

[16] J.-H. Jung, "Bifilar winding of a center-tapped transformer including integrated resonant inductance for LLC resonant converters," *IEEE Trans. Power Electron.*, vol. 28, no. 2, pp. 615–620, Feb. 2013, doi: 10.1109/TPEL.2012.2213097.

[17] B. Li, Q. Li, and F. C. Lee, "High-frequency PCB winding transformer with integrated inductors for a bi-directional resonant converter," *IEEE Trans. Power Electron.*, vol. 34, no. 7, pp. 6123–6135, Jul. 2019, doi: 10.1109/TPEL.2018.2874806.

[18] J. Li et al., "Matrix inductor-transformer integration and optimization design for CLLC bidirectional resonant converter," *Proc. Chin. Soc. Elect. Eng.*, vol. 42, no. 10, pp. 3720–3728, 2022.

[19] J. S. Knoll, G. Son, C. DiMarino, Q. Li, H. Stahr, and M. Morianz, "A PCB-embedded 1.2 kV SiC MOSFET half-bridge package for a 22 kW AC–DC converter," *IEEE Trans. Power Electron.*, vol. 37, no. 10, pp. 11927–11936, Oct. 2022, doi: 10.1109/TPEL.2022.3177369.

[20] A. Nabih, F. Jin, R. Gadelrab, F. C. Lee, and Q. Li, "Characterization and mitigation of dimensional effects on core loss in high-power high-frequency converters," *IEEE Trans. Power Electron.*, vol. 38, no. 11, pp. 14017–14036, Nov. 2023, doi: 10.1109/TPEL.2023.3285633.

Tianlong Yuan (Graduate Student Member, IEEE) received the B.S. degree in electrical engineering from Harbin Institute of Technology, Harbin, China, in 2019. He is currently working toward the Ph.D. degree in electrical engineering with the Center for Power Electronics Systems, Virginia Tech, Blacksburg, VA, USA.

His research interests include EV charging, bidirectional power conversion, and integrated planar magnetics.

Feng Jin (Member, IEEE) received the B.Sc. and M.Sc. degrees from the Nanjing University of Aeronautics and Astronautics, Nanjing, China, in 2012 and 2015, respectively, and the Ph.D. degree from Virginia Tech, Blacksburg, VA, USA, in 2024, all in electrical engineering.

He is currently a member of the R&D team of Delta Electronics Americas Ltd. From March 2024 to May 2024, he was a Research Associate with the Center for Power Electronics Systems, Virginia Tech, Blacksburg, VA, USA. From 2015 to 2019, he was an Electrical Engineer with Delta Electronics, Hangzhou, China. His research interests include EV charging, bidirectional power conversion, and planar magnetics.

Dr. Jin was the recipient of the Best Presentation Awards at IEEE Applied Power Electronics Conference and Exposition in 2023 and 2024.

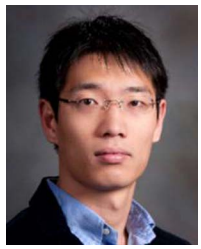

Qiang Li (Member, IEEE) received the B.S. and M.S. degrees in power electronics from Zhejiang University, Hangzhou, China, in 2003 and 2006, respectively, and the Ph.D. degree in electrical engineering from Virginia Tech, Blacksburg, VA, USA, in 2011.

He is currently a Professor with the Center for Power Electronics Systems at Virginia Tech. He holds 37 U.S. patents and has authored or coauthored 185 refereed technical articles. His current research interests include power management for distributed power systems, applications of wide-bandgap power devices, high-frequency power conversion and controls, magnetics and electromagnetic interference, high-density electronics packaging and integration, and renewable energy.

Dr. Li received the First Place Prize Article Award of IEEE TRANSACTIONS ON POWER ELECTRONICS in 2016. He was also a recipient of the 2017 U.S. National Science Foundation Career Award.